



Trans. Nonferrous Met. Soc. China 33(2023) 839-850

Transactions of Nonferrous Metals Society of China

www.tnmsc.cn



# Hot deformation behaviour and microstructure evolution of gold-imitation brass alloy with high corrosion resistance

Xiang-yu YU, Zhu XIAO, Zhou LI, Xin-si ZHAO, Si-jian LU, Yuan-yuan FU
School of Materials Science and Engineering, Central South University, Changsha 410083, China
Received 26 October 2021; accepted 19 November 2022

**Abstract:** The hot deformation characteristics of Cu-13Zn-1Ni-1Sn-1.5Al gold-imitation brass alloy in a temperature range from 953 to 1123 K and a strain rate range from 0.001 to 1 s<sup>-1</sup> were investigated by hot compression tests. The stress-strain curves show that the flow stress decreases with the increase of temperature and the decrease of strain rate. The dynamic recrystallization grains appear while the temperature reaches 1073 K at a constant strain rate of 0.01 s<sup>-1</sup>. The constitutive equation of the alloy was established and its deformation activation energies were obtained at different strains ( $\varepsilon$ =0.1, 0.2, 0.3, 0.4, 0.5, 0.6, 0.7, 0.8). When the strain is 0.8, the constitutive equation of the alloy is  $\dot{\varepsilon}$  = 7.22×10<sup>9</sup>[sinh(0.0187 $\sigma$ )]<sup>3.67</sup>exp[-227.17/(RT)], and the deformation activation energy is 227.17 kJ/mol. The dissipation power maps and instability maps were established at different strains, which suggested that the recommended processing condition for hot compression was in the temperature range of 1010–1040 K with a strain rate of 1 s<sup>-1</sup>. **Key words:** gold-imitation brass alloy; hot deformation behaviour; dynamic recovery; dynamic recrystallization

### 1 Introduction

Copper alloys have been widely used in electronic, chemical, mechanical, architectural and decorative fields because of their excellent electrical and thermal conductivities, high strength and nice corrosion resistance [1-4]. Due to the great golden brightness and unique antibacterial properties, gold-imitation copper alloys have been widely used in the field of decoration [5]. Many gold-imitation copper alloys are also used as the coinage, such as H7211 for Chinese coinage, Cu5Zn5Al1Ni for Nordic coinage and Cu10Zn6Al for Australian coinage [6,7]. Cu-13Zn-1Ni-1Sn-1.5Al (CZNS-Al) gold-imitation brass alloys designed by our group have better golden brightness and corrosion resistance performance than H7211 alloy [8]. In the manufacturing process of the metal strips for coinage, the billet produced by semi-continuous casting is transformed into the strip using hot rolling. However, the improper hot processing parameters would form the heterogeneous microstructures in the strip [9,10]. This reduces the corrosion resistance and mechanical properties of the alloy and limits its application [8]. Therefore, it is necessary to study the hot deformation behaviour of gold-imitation brass alloy.

The processing map plays a very important role in guiding the planning of the metal thermal processing technology. The hot deformation behaviour of the alloy is usually affected by strain rate and deformation temperature [11–13]. ZHU et al [14] developed a processing map of Cu–Zn–Al–Ni–Me–Re, and concluded that the instability of the alloy would occur in two regions. The deformation temperature of the first region is at 650–670 °C with strain rates of 0.1–1 s<sup>-1</sup>, and the second one is at 740–770 °C with strain rates of 0.32–1 s<sup>-1</sup> [14]. The hot deforming processing map was established from hot compression experiment results [15–17]. In order to obtain the designed gold-

imitation brass alloy with anisomeric microstructures and excellent hot-working property, hot compression experiment was carried out.

hot In this study, the deformation characteristics of Cu-13Zn-1Ni-1Sn-1.5Al goldimitation brass alloy were systematically studied in a temperature range from 953 to 1123 K and a strain rate range from 0.001 to 1 s<sup>-1</sup>. The constitutive model of the alloy was optimized by friction correction and temperature correction. The processing map was also established, and the microstructure evolution of the alloy during hot deformation was revealed by metallographic microscopy and transmission electron microscopy.

## 2 Experimental

The ingot of the designed gold-imitation brass alloy of Cu-13Zn-1Ni-1Sn-1.5Al was prepared in a medium-frequency induction furnace using highly pure metals (>99.9%). The defect of ingot was removed by milling. The ingot was homogenized at 858 K for 6.5 h, then at 963 K for 3 h, and finally at 1043 K for 3 h. The hot compression samples with a diameter of 8 mm and a height of 12 mm were prepared using a wire EDM machine. Additionally, mechanical polishing was used to polish the surface of the samples.

The hot compression tests were carried out on a Gleeble–3500 thermo-simulator at different temperatures of 953, 983, 1013, 1043, 1073 and 1123 K, respectively. The strain rate was set as 0.001, 0.01, 0.1 and 1 s<sup>-1</sup>, respectively. The heating rate was 5 °C/s. Samples were hold at the specific deformation temperature for 3 min and then compressed to a total true strain of 0.85. In order to reduce friction and uneven deformation, a lubricant (75 wt.% graphite + 20 wt.% engine oil + 5 wt.% trimethylbenzene nitrate) was applied to the shallow grooves at both ends of each sample before compression.

The deformed samples were cut along the compression direction, and the microstructure of the alloy was observed by metallographic microscopy (OM) and transmission electron microscopy (TEM). The OM specimens were mechanically polished and etched by a solution (5 g FeCl<sub>3</sub>, 25 mL HCl and 75 mL deionized water). The OM observation was conducted on a Leica DM6000M microscope. The

TEM specimens were mechanically polished to  $70-100 \, \mu m$  and then electro-polished by the Struers Tenupol-5 electrolytic instrument using an electron-polishing solution with 30 vol.% nitric acid and 70 vol.% methanol in temperature range from -30 to -20 °C. The TEM observation was conducted on a Tecnai  $G^2$  F20 instrument.

### 3 Result and discussion

### 3.1 Correction of stress-strain curve

### 3.1.1 Friction correction

The heterogeneity of deformation process and inaccuracy of stress measurement are related to the friction between samples and fixture. The drum-like samples are obtained after hot compression tests. Figure 1 shows the schematic diagrams of the alloy samples before and after deformation. The error of stress caused by friction is corrected by the following equation [18]:

$$\frac{P_{\rm e}}{\sigma} = \frac{8bR_{\rm e}}{H_{\rm e}} \left\{ \left[ \frac{1}{12} + \left( \frac{H_{\rm e}}{R_{\rm e}b} \right)^2 \right]^{3/2} - \left( \frac{H_{\rm e}}{R_{\rm e}b} \right)^3 - \frac{\mu e^{-b/2}}{24\sqrt{3} \left( e^{-b/2} - 1 \right)} \right\} \tag{1}$$

where  $P_e$  is uncorrected stress given by hot compression test,  $\sigma$  is stress after friction, b is barrel parameter,  $\mu$  is friction coefficient, and  $R_e$  and  $H_e$  are equivalent values of radius and height of samples, respectively.

 $R_{\rm e}$  and  $H_{\rm e}$  are represented as

$$R_{e} = R_{0} \exp\left(-\dot{\varepsilon}/2\right) \tag{2}$$

$$H_e = h_0 \exp(-\dot{\varepsilon}) \tag{3}$$

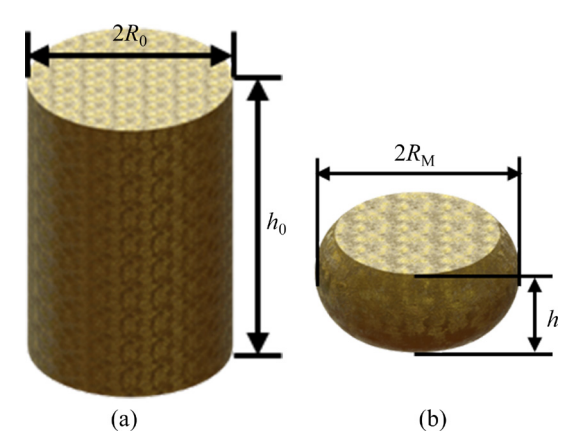


Fig. 1 Schematic diagrams of alloy samples before (a) and after (b) hot compression test

where  $R_0$  and  $h_0$  are radius and height before deformation, respectively and  $\dot{\varepsilon}$  is strain rate of hot deformation.

The constant friction coefficient is expressed as

$$\mu = \frac{R_{\rm f}}{h} \cdot \frac{3\sqrt{3}b}{12 - 2b} \tag{4}$$

where  $R_f$  and h are average radius and height of the sample after deformation, respectively.

 $R_{\rm f}$  and b are evaluated by the following equations:

$$R_{\rm f} = R_0 \sqrt{\frac{h_0}{h}} \tag{5}$$

$$b=4\frac{R_{\rm M}-R_{\rm T}}{R_{\rm f}}\cdot\frac{h}{h_0-h}\tag{6}$$

where  $R_{\rm M}$  and  $R_{\rm T}$  are maximum radius and top radius of deformed samples, respectively.  $R_{\rm T}$  is obtained as

$$R_{\rm T} = \sqrt{3\frac{h_0}{h}R_0^2 - 2R_{\rm M}^2} \tag{7}$$

The modified stress is calculated by Eq. (1).

## 3.1.2 Temperature correction

In the hot compression tests, if the strain rate is too high, the temperature change of the sample cannot be obtained by the sensor in time. Therefore, the effective temperature is corrected by the following formula [19]:

$$\Delta T = \frac{0.95 f}{\rho c_p} \int_0^{\varepsilon} \sigma d\varepsilon \tag{8}$$

where  $\Delta T$  is the change in temperature, f is the adiabatic correction factor, and defined as 0, 0.25, 0.5, 0.75 at strain rates of 0.001, 0.01, 0.1 and 1 s<sup>-1</sup> [20], respectively,  $\rho$  is the density of samples (8.25 g/cm<sup>3</sup>), and  $c_p$  is the specific heat capacity (0.38 J/(g·K) for H85 brass).

The calculated temperature changes during hot compression tests at different temperatures and strain rates are shown in Fig. 2. The  $\Delta T$  decreases with the increase of deformation temperature under the same true strain.

The relationships among the temperature, flow stress and strain rate are expressed by Arrhenius equations. The influence of the temperature and strain rate on deformation behaviour is expressed by Zener–Hollomon parameter [21,22]:

$$Z = A_1 \sigma^n = \dot{\varepsilon} \exp[Q/(RT)], \quad \alpha \sigma < 0.8 \tag{9}$$

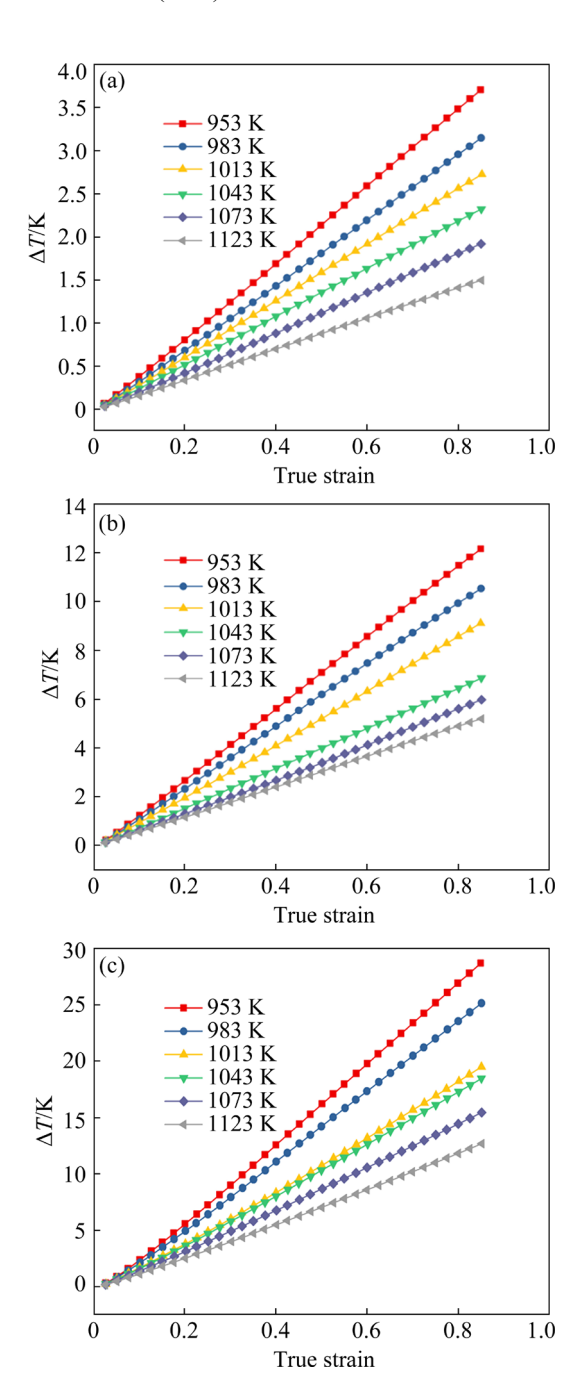


**Fig. 2** Temperature changes of designed alloy deformed at different temperatures and strain rates: (a)  $0.01 \text{ s}^{-1}$ ; (b)  $0.1 \text{ s}^{-1}$ ; (c)  $1 \text{ s}^{-1}$ 

$$Z = A_2 \exp(\beta \sigma) = \dot{\varepsilon} \exp[Q/(RT)], \quad \alpha \sigma > 1.2$$
 (10)

$$Z = A_3 \left[ \sinh(\alpha \sigma) \right]^m = \dot{\varepsilon} \exp[Q/(RT)]$$
 (11)

where Z is Zener–Hollomon parameter, R is the molar gas constant (8.314 J/(mol·K)), T is the thermodynamic temperature (K), Q is the activation energy (kJ/mol),  $A_1$ ,  $A_2$ ,  $A_3$ ,  $\alpha$ ,  $\beta$ , n and m are the material constants, respectively, and  $\alpha = \beta/n$  [23]. Under low stress condition, the relationships among

the temperature, flow stress and strain rate are obtained by Eq. (9). Under high stress condition, the relationships among the temperature, flow stress and strain rate are obtained by Eq. (10). Additionally, Eq. (11) is suitable for the whole stress condition [21].

The correction of flow stress is finished by linearly fitting the true stress value and the corresponding corrected temperature. Figure 3 shows the linear relationships of  $\ln \sigma - T^{-1}$  and  $\sigma - T^{-1}$ . And the true stress at the set temperature is gained by extrapolation method.

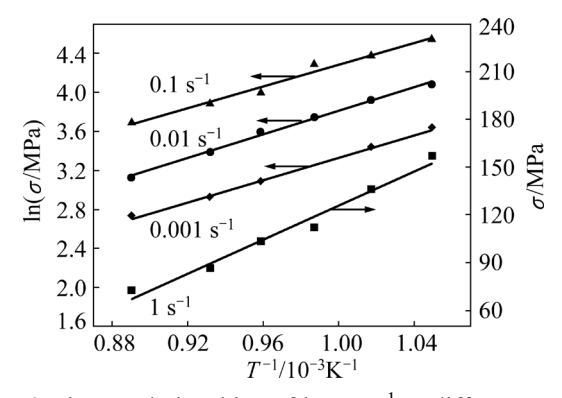


**Fig. 3** Linear relationships of  $\ln \sigma - T^{-1}$  at different strain rates and  $\sigma - T^{-1}$  at strain rate of 1 s<sup>-1</sup>

True stress-true strain curves of the alloy with and without the friction and temperature corrections are shown in Fig. 4. The corrected stress is lower than the uncorrected one at each deformation temperature and a stable rheological behaviour occurs. The hot deformation behaviour of the designed alloy is sensitive to the deformation parameters. The flow stress increases rapidly at the early stage of deformation, and then it is almost unchanged with the further increase of the strain. When the sample is deformed at 1123 K with the strain rate of 0.001 s<sup>-1</sup>, the flow stress of the sample is about 15 MPa. The flow stress at 1123 K is much lower than that at 953 K (about 40 MPa). The flow stress decreases significantly with the increase of the deformation temperature.

### 3.2 Activation energy and constitutive equations

Taking the natural logarithms of Eqs. (9)–(11), we have

$$\ln \dot{\varepsilon} = n \ln \sigma - Q/(RT) + \ln A_1 \tag{12}$$

$$\ln \dot{\varepsilon} = \beta \sigma - Q/(RT) + \ln A_2 \tag{13}$$

$$\ln \dot{\varepsilon} = m \ln[\sinh(\alpha \sigma)] - Q/(RT) + \ln A_3 \tag{14}$$

$$\ln Z = m \ln[\sinh(\alpha \sigma)] + \ln A_3 \tag{15}$$

According to Eq. (14), activation energy is rewritten as follows:

$$Q=1000R \left\{ \frac{\partial \ln \dot{\varepsilon}}{\partial \ln[\sinh(\alpha\sigma)]} \right\}_{T}.$$

$$\left\{ \frac{\partial \ln[\sinh(\alpha\sigma)]}{\partial (1000/T)} \right\}_{\dot{\varepsilon}} = 1000Rms$$
(16)

The linear relationship of  $\ln \dot{\varepsilon} - \ln \sigma$ ,  $\ln \dot{\varepsilon} - \sigma$ ,  $\ln \dot{\varepsilon} - \ln[\sinh(\alpha\sigma)]$  and  $\ln[\sinh(\alpha\sigma)] - T^{-1}$  of the sample at various deformation temperatures with the strain of 0.8 are shown in Fig. 5. n,  $\beta$ , m and s are the average slops of the plotted lines in Figs. 5(a–d), respectively. The average slopes are calculated according to Fig. 5, and the result shows that n=4.88,  $\beta$ =0.0914 MPa<sup>-1</sup>,  $\alpha$ =0.0187 MPa<sup>-1</sup>, m=3.67 and s=7.44. According to Eq. (16), the deformation activation energy of the alloy at the strain of 0.8 is 227.17 kJ/mol.

The fitted relationship between  $\ln Z$  and  $\ln[\sinh(\alpha\sigma)]$  is shown in Fig. 6, which indicates a typical linear dependence. According to Eq. (15), the intercept of the line,  $\ln A_3$ , is 22.7. The constitutive equation of the gold-imitation brass alloy at the strain of 0.8 is expressed as

$$\dot{\varepsilon} = 7.22 \times 10^{9} \left[ \sinh(0.0187\sigma) \right]^{3.67} \exp[-227.17/(RT)]$$
(17)

As shown in Fig. 7, the values of  $\alpha$ , m, Q and  $\ln A_3$  are obtained by linearly fitting of the experimental data at different true strains ( $\varepsilon$ =0.1, 0.2, 0.3, 0.4, 0.5, 0.6, 0.7, and 0.8). The relationships between  $\alpha$ , m, Q,  $\ln A_3$  and the true strain are fitted by six polynomial functions, respectively, which are shown as follows:

$$\alpha(\varepsilon) = B_0 + B_1 \varepsilon + B_2 \varepsilon^2 + B_3 \varepsilon^3 + B_4 \varepsilon^4 + B_5 \varepsilon^5 + B_6 \varepsilon^6$$
(18)

$$m(\varepsilon) = C_0 + C_1 \varepsilon + C_2 \varepsilon^2 + C_3 \varepsilon^3 + C_4 \varepsilon^4 + C_5 \varepsilon^5 + C_6 \varepsilon^6$$
(19)

$$Q(\varepsilon) = D_0 + D_1 \varepsilon + D_2 \varepsilon^2 + D_3 \varepsilon^3 + D_4 \varepsilon^4 + D_5 \varepsilon^5 + D_6 \varepsilon^6$$
(20)

$$\ln A_3(\varepsilon) = E_0 + E_1 \varepsilon + E_2 \varepsilon^2 + E_3 \varepsilon^3 + E_4 \varepsilon^4 + E_5 \varepsilon^5 + E_6 \varepsilon^6$$
(21)

The fitting results are listed in Table 1. The constitutive equation under specific strain is expressed as

$$\sigma = \frac{1}{\alpha} \sinh^{-1} \left[ \frac{\dot{\varepsilon} \exp[Q/(RT)]}{A_3} \right]^{1/m}$$
 (22)

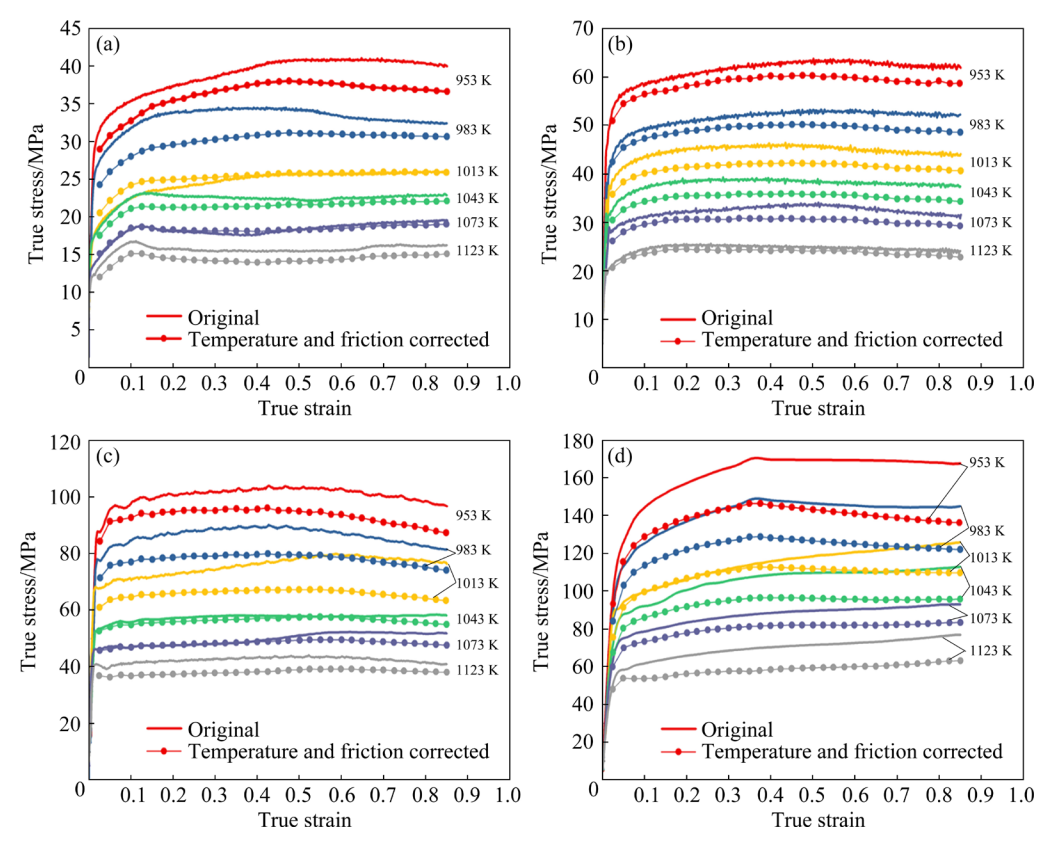


**Fig. 4** True stress—true strain curves of alloy with and without friction and temperature correction at different strain rates: (a) 0.001 s<sup>-1</sup>; (b) 0.01 s<sup>-1</sup>; (c) 0. 1 s<sup>-1</sup>; (d) 1 s<sup>-1</sup>

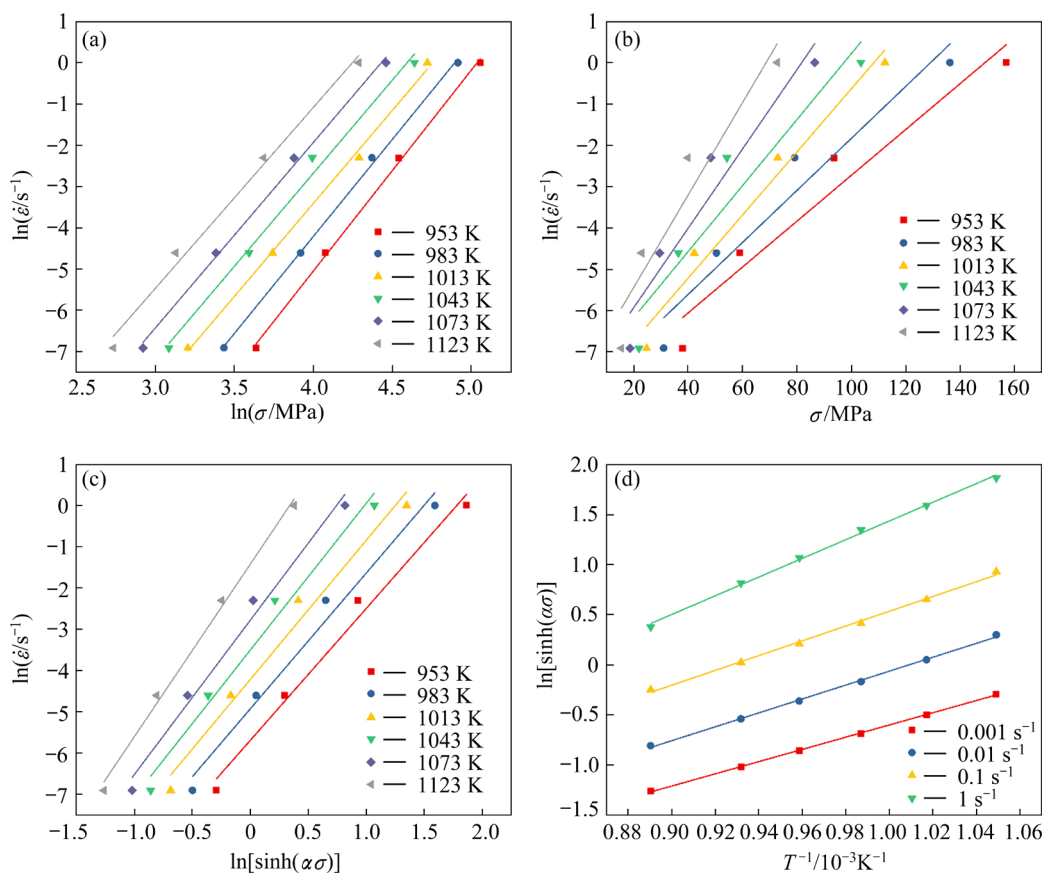


**Fig. 5** Linear relationships of  $\ln \dot{\varepsilon} - \ln \sigma$  (a),  $\ln \dot{\varepsilon} - \sigma$  (b),  $\ln \dot{\varepsilon} - \ln[\sinh(\alpha\sigma)]$  (c), and  $\ln[\sinh(\alpha\sigma)] - T^{-1}$  (d) of sample at various deformation temperatures and strain of 0.8

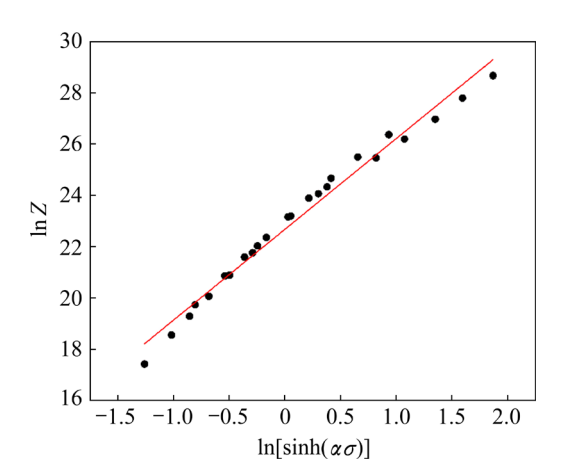


**Fig. 6** Fitted linear relationship between  $\ln Z$  and  $\ln[\sinh(\alpha\sigma)]$ 

Using the data listed in Table 1 and Eq. (22), the true stress under the specific true strain of the designed alloy is calculated and shown in Fig. 8, and the experimental data under the specific true strain are also shown in Fig. 8. In most conditions, the calculated data fit well with the experimental data.

# 3.3 Optical microscopy observation of hotdeformed sample

Figure 9 shows the microstructures of the alloy deformed at different temperatures and strain rates. Figures 9(a) and (b) show the microstructures of the alloy deformed at 953 K with strain rates of 0.1 and  $1 \text{ s}^{-1}$ , respectively. With the increase of strain rate,

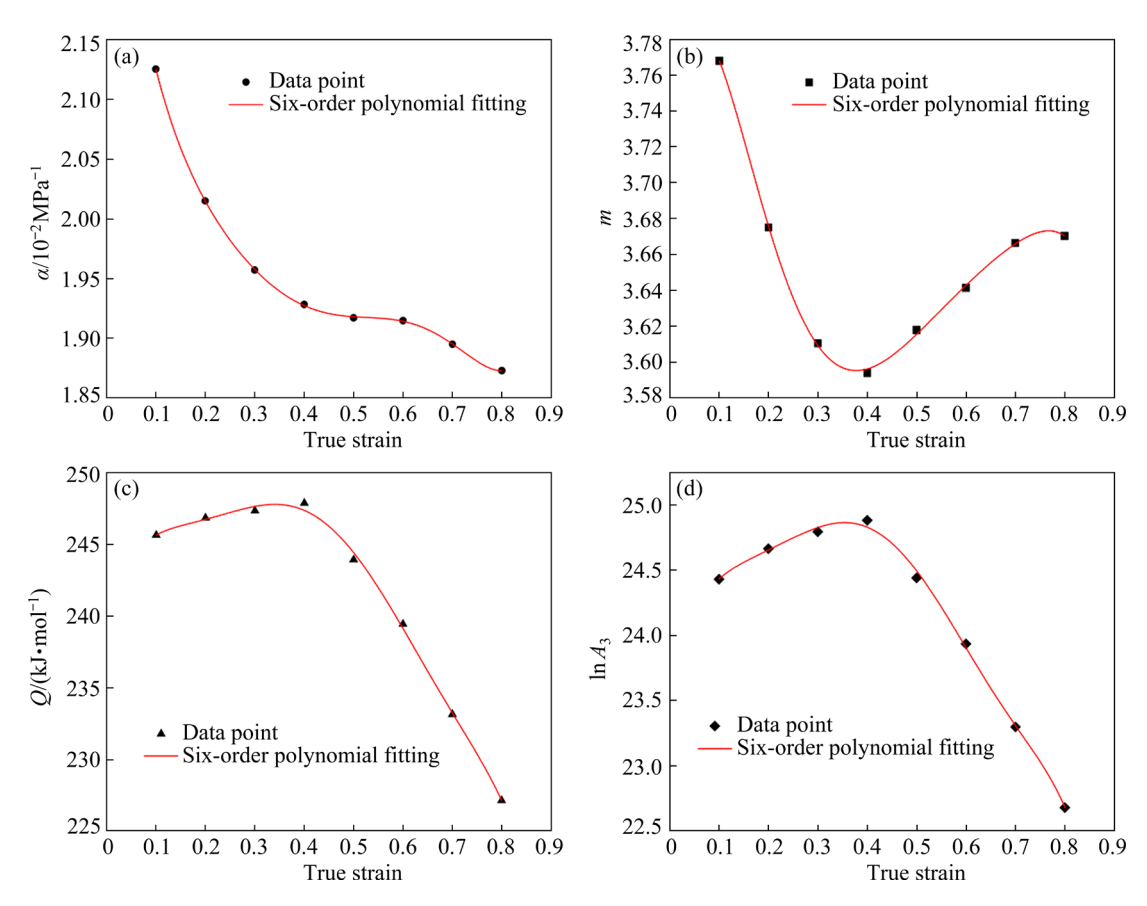
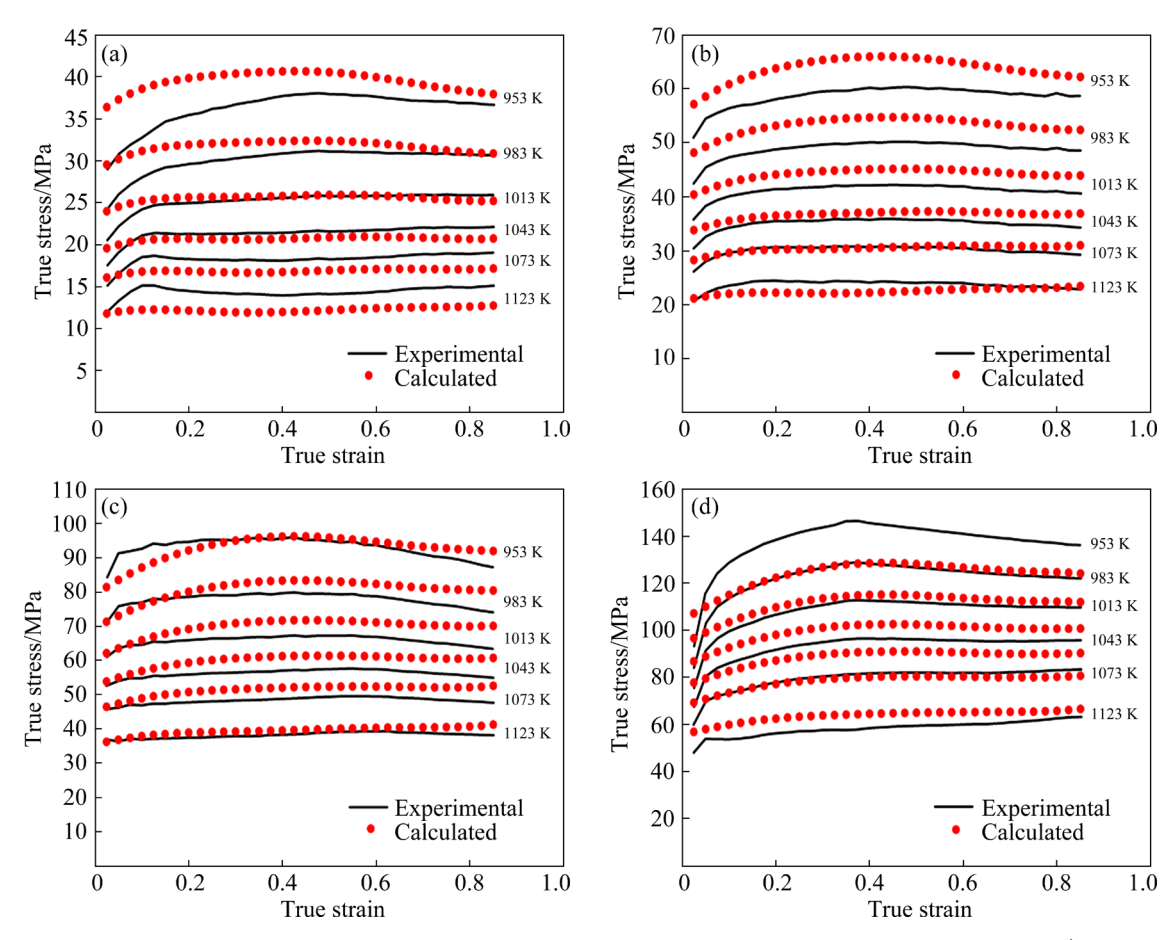


Fig. 7 Six polynomial fitting curves of  $\alpha$  (a), m (b), Q (c) and  $\ln A_3$  (d)

**Table 1** Results of six polynomial function fitting

Table 1 Results of the polynomial remetion menig			
α	m	Q	$\ln A_3$
$B_0=2.40116$	$C_0$ =3.73526	$D_0 = 240.0017$	$E_0$ =23.56219
$B_1 = -4.35076$	$C_1$ =1.96388	$D_1$ =121.50051	$E_1 = 17.70392$
$B_2 = 21.67251$	$C_2 = -23.74652$	$D_2 = -995.16144$	$E_2 = -137.31147$
$B_3 = -69.04895$	$C_3$ =87.43167	$D_3$ =4302.41263	$E_3 = 590.96861$
$B_4 = 128.71404$	$C_4 = -149.69481$	$D_4$ =-9353.38265	$E_4 = -1297.69167$
$B_5 = -124.02531$	$C_5 = 125.20711$	$D_5 = 9455.20854$	$E_5 = 1335.98125$
$B_6 = 47.12805$	$C_6 = -41.64128$	$D_6$ =-3597.69149	$E_6 = -518.72917$



**Fig. 8** Comparison of experimental and calculated flow stress at different strain rates: (a)  $0.001 \text{ s}^{-1}$ ; (b)  $0.01 \text{ s}^{-1}$ ; (c)  $0.1 \text{ s}^{-1}$ ; (d)  $1 \text{ s}^{-1}$ 

more shear bands and smaller grains appear, as shown in Fig. 9(b) [24]. Figure 9(c) shows the microstructure of the alloy deformed at 1013 K with the strain rate of 0.01 s<sup>-1</sup>. Figures 9(d) and (e) show the microstructures of the alloy deformed at 1073 K with strain rates of 0.01 and  $1 \text{ s}^{-1}$ , respectively. A "necklace" structure caused by discontinuous dynamic recrystallization (DRX) appears when the alloy is deformed at 1013 K with the strain rate of  $0.01 \text{ s}^{-1}$  [25]. With the increase of the deformation temperature to 1073 K, the completely recrystallized structure of the alloy is observed. The necklace-like structure is formed when the strain rate increases to  $1 \text{ s}^{-1}$  (as shown in Fig. 9(e)). The new DRX grains mainly nucleate at the deformed grain boundaries. The necklace-like structure and the DRX grains along the zigzag high-angle grain boundary are formed strain-induced boundary migration [17,26]. A small number of DRX grains are also observed inside the deformed grains, which are formed by the subgrain boundary migration or sub-grain boundary

aggregation under high strain values [26]. As a result, the DRX of the alloy tends to occur at high deformation temperature or low strain rate.

### 3.4 TEM observation of hot-deformed sample

Figure 10 shows the TEM images of the samples deformed under different conditions. The microstructure of the sample, which is deformed at the temperature of 953 K with strain rate of  $0.001 \text{ s}^{-1}$ , is shown in Figs. 10(a) and (b). The density in the alloy dislocation Recrystallized grains are formed by discontinuous dynamic recrystallization during hot deformation process [27]. Figures 10(c) and (d) show the microstructure of the sample deformed at 953 K with strain rate of 0.1 s<sup>-1</sup>. When the strain rate increases to 0.1 s<sup>-1</sup> the dislocation density in the alloy increases significantly. A large number of dislocations tangle with each other, and dislocation movement leads to the formation of dislocation cells. Subgrains are formed during dynamic recovery process. When the deformation temperature

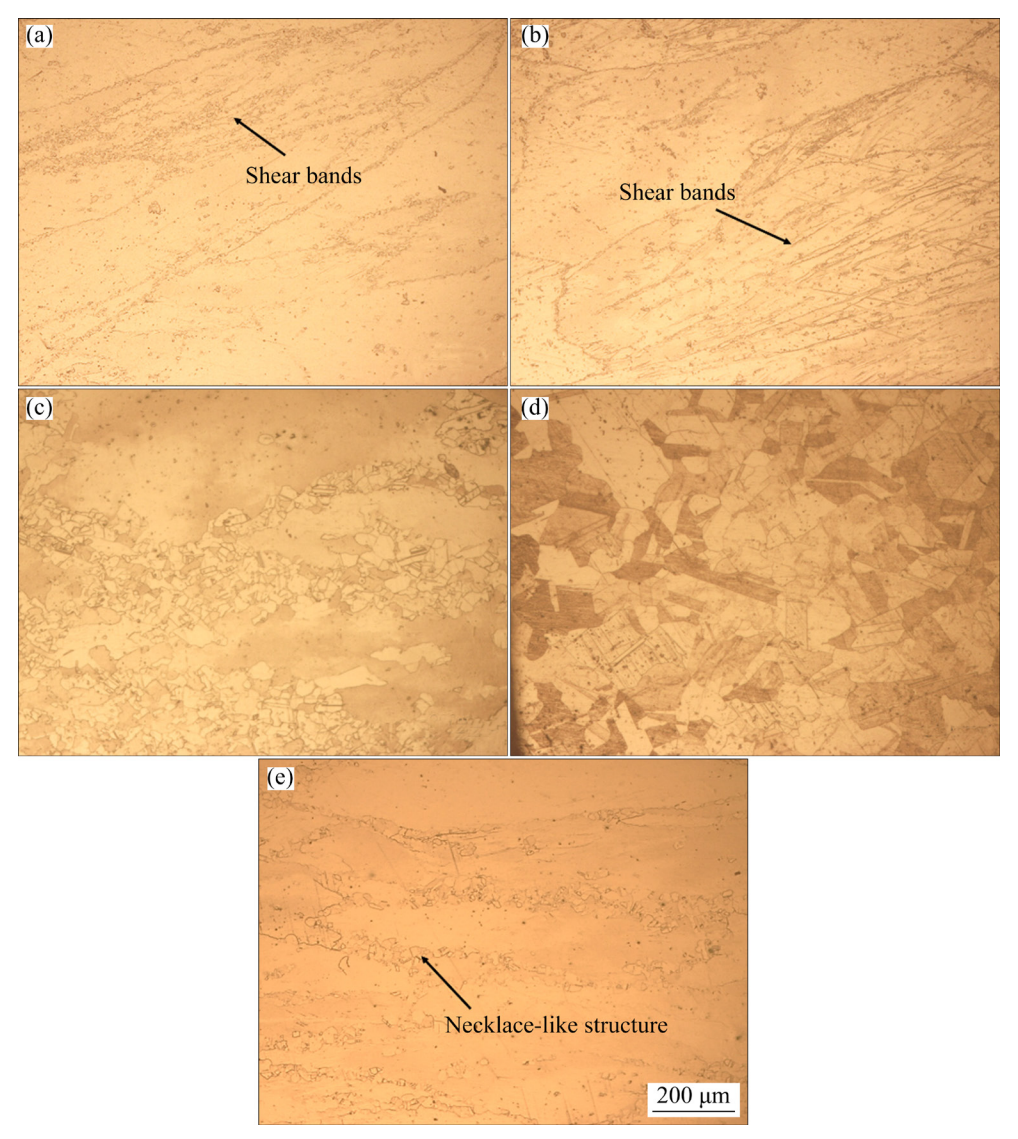


**Fig. 9** Hot compression microstructures of alloy deformed at different temperatures and strain rates: (a) 953 K,  $0.1 \text{ s}^{-1}$ ; (b) 953 K,  $1 \text{ s}^{-1}$ ; (c) 1013 K,  $0.01 \text{ s}^{-1}$ ; (d) 1073 K,  $0.01 \text{ s}^{-1}$ ; (e) 1073 K,  $1 \text{ s}^{-1}$ 

rises to 1073 K, DRX grains with smooth and straight grain boundaries appear, as shown in Fig. 10(e).

### 3.5 Processing map

According to the dynamic materials model, workpiece is considered as a power dissipater [28]. The total absorbing power (P) is separated into power dissipation by plastic work (G) and power dissipation by microstructure evolution (J), which is expressed as follows [28]:

$$P = \sigma \dot{\varepsilon} = G + J = \int_{0}^{\dot{\varepsilon}} \sigma d\dot{\varepsilon} + \int_{0}^{\sigma} \dot{\varepsilon} d\sigma$$
 (23)

The relationship between G and J is expressed by the parameter i (the strain rate sensitivity index) [29]:

$$i = \frac{\mathrm{d}J}{\mathrm{d}G} = \left[ \frac{\partial (\ln \sigma)}{\partial (\ln \dot{\varepsilon})} \right]_{c,T} \tag{24}$$

J is calculated by strain rate sensitivity index i and strain rate  $\dot{\varepsilon}$ :

$$J = \sigma \dot{\varepsilon} - \int_{0}^{\dot{\varepsilon}} K \dot{\varepsilon}^{i} d\dot{\varepsilon} = \left[ i/(i+1) \right] \sigma \dot{\varepsilon}$$
 (25)

where *K* is the material constant.

With an ideal linear dissipation, i=1,  $J=J_{\text{max}}=\sigma\dot{\epsilon}/2$ . The efficiency of power dissipation  $(\eta)$  is written as

$$\eta = \frac{J}{J_{\text{max}}} = \frac{2i}{i+1} \tag{26}$$

Based on the principle of irreversible thermodynamic extremum, PRASAD et al [28] deduced the criterion of continuous instability of materials

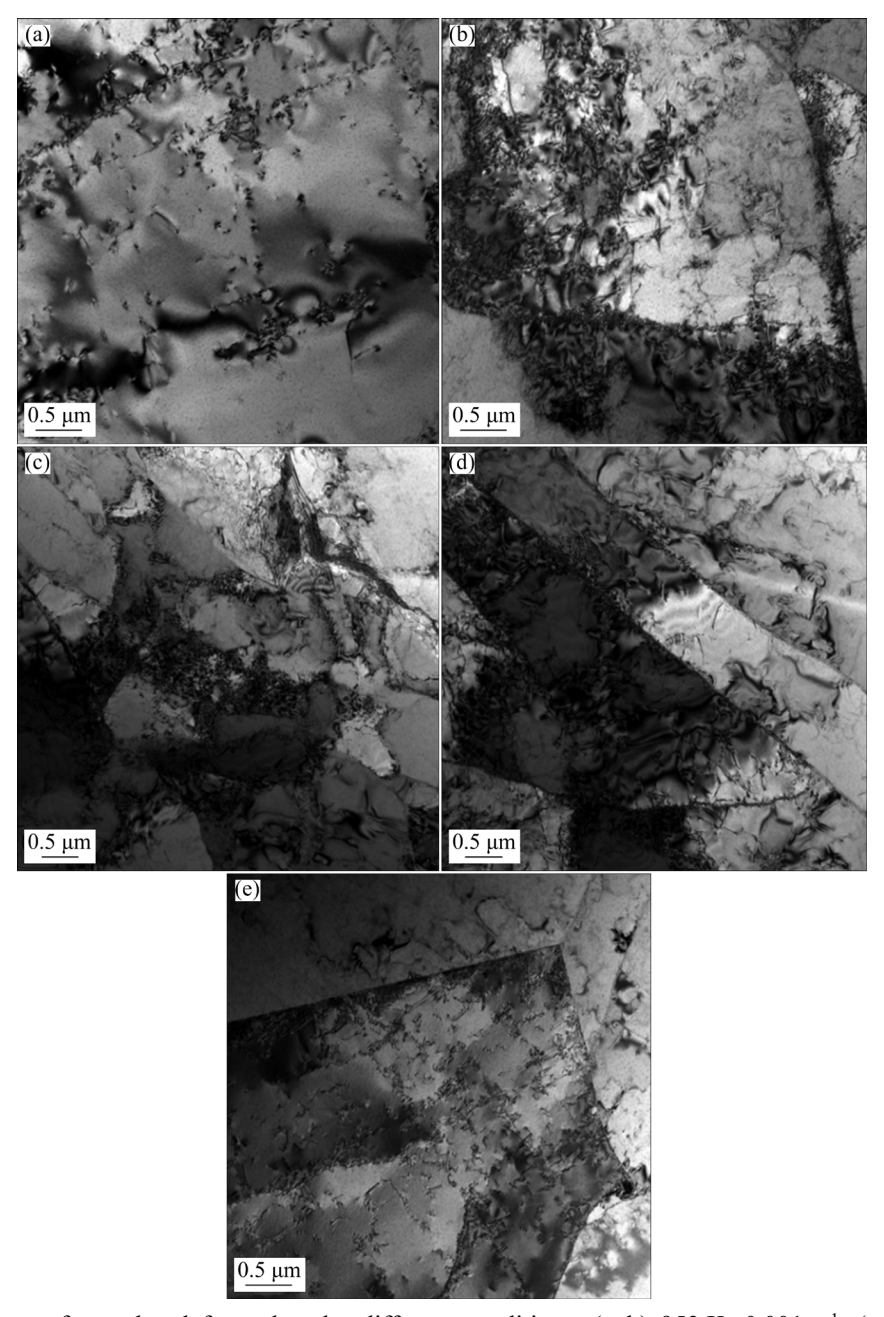


**Fig. 10** TEM images of samples deformed under different conditions: (a, b) 953 K,  $0.001 \text{ s}^{-1}$ ; (c, d) 953 K,  $0.1 \text{ s}^{-1}$ ; (e) 1073 K,  $0.01 \text{ s}^{-1}$ 

during plastic deformation. The instability criterion is expressed by dimensionless parameter  $\xi(\dot{\varepsilon})$ , which is calculated as [30]

$$\xi(\dot{\varepsilon}) = \frac{\partial \ln[i/(i+1)]}{\partial \ln \dot{\varepsilon}} + i < 0 \tag{27}$$

Figure 11 shows the power dissipation diagrams and the rheological instability diagrams of the designed alloys with strains of 0.55 and 0.85, respectively. When the strain is 0.55, there are two regions with the highest dissipation efficiency. One is that the deformation temperature of the alloy is

between 1010 and 1060 K and the strain rate is  $1 \, \mathrm{s}^{-1}$ . The other is that the temperature is between 1060 and 1120 K and the strain rate is  $0.001 \, \mathrm{s}^{-1}$ . The value of  $\xi(\dot{\varepsilon})$  is higher than zero in the instability diagram of the alloy. It can be inferred that when the strain is 0.55, there is no instability zone in the alloy at the specific temperature and strain rate. When the strain is 0.85, the alloy reaches the highest power dissipation efficiency of 43% in the temperature range of 1000–1040 K with the strain rate of  $1 \, \mathrm{s}^{-1}$ . Similarly, the value of  $\xi(\dot{\varepsilon})$  is always greater than zero. No instability zone exists for the

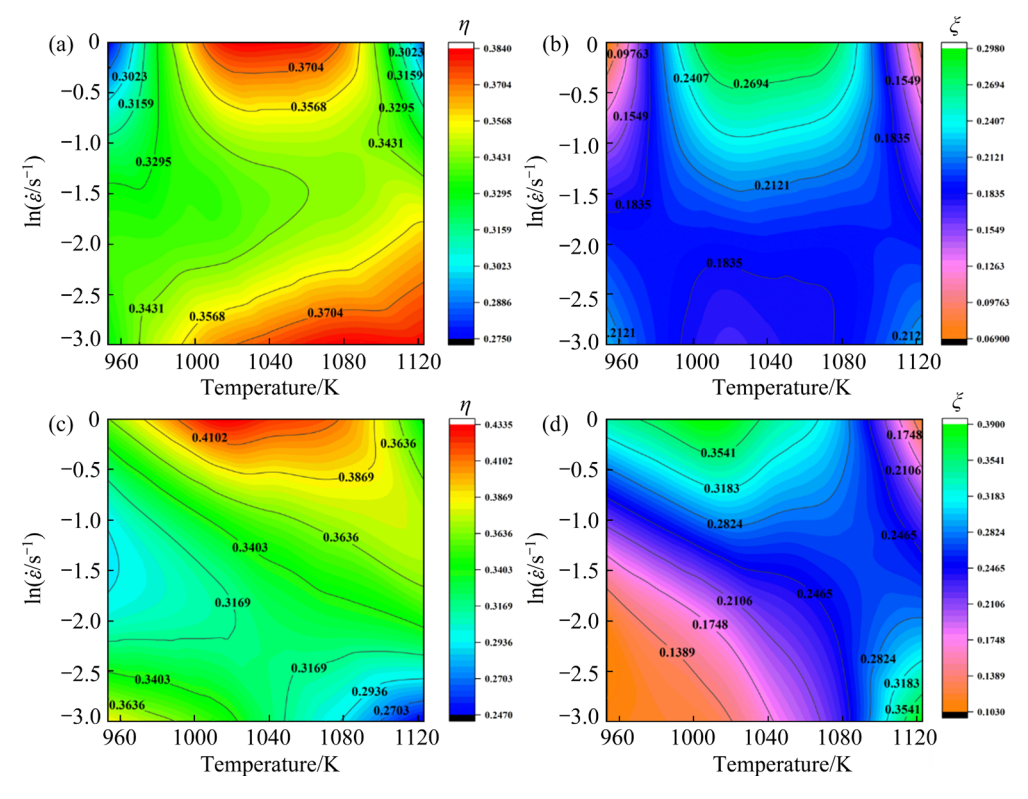


Fig. 11 Power dissipation diagrams (a, c) and rheological instability diagrams (b, d) of designed alloys at different strains: (a, b)  $\varepsilon$ =0.55; (c, d)  $\varepsilon$ =0.85

alloy at the experimental temperature and strain rate. In summary, the designed alloy has the best hot workability when it is deformed under the conditions of 1010-1040 K and  $1 \text{ s}^{-1}$ .

### 4 Discussion

In this work, the hot deformation behaviour and microstructure evolution of the designed goldimitation brass alloy were studied. By correcting the friction and temperature, the stress-strain curves were adjusted. The characteristics of stress-strain curve are as follows: (1) in the initial stage of deformation, the stress increases rapidly due to the quick multiplication of dislocation; (2) for specific strain rate, the stress increases slowly after reaching the peak point; (3) the flow stress increases with the increase of strain rate and decreases with the increase of temperature for all samples. The competition between work hardening and dynamic softening is the key reason for the change of flow stress during hot deformation. High temperature thermal activation results in dynamic softening, and low strain rate provides enough time for the softening [31,32].

When the designed alloy was deformed at 953 K with high strain rate of 1 s<sup>-1</sup>, the DRX grains and cell structures occurred due to the dislocation climbing, cross-slipping, and annihilation of unlike dislocation. When the strain rate decreased to  $0.01 \, \rm s^{-1}$ , high-angle grain boundaries were transformed by thermal activation, and the number of recrystallizing grains increased. During high temperature deformation, the cross-slip of screw dislocations and the climbing of edge dislocation occurred, the subgrain boundary annihilated, the regular boundaries formed, and the stored energy in the dislocation and at subgrain boundary was consumed.

The constitutive equation and processing map of the designed alloy during hot deformation were established. When copper alloys, such as Cu-Ti-Zr, Cu-Ni-Sn and Cu-Zn-Al-Ni-Me-Re alloys, are deformed in a wide temperature range of 973–1123 K and strain rate range of 0.001–1 s<sup>-1</sup>, there are instability zones [14–16]. However, the designed Cu-13Zn-1Ni-1Sn-1.5Al alloy shows excellent processing performance in wide ranges of temperature and strain rate. According to the rheological instability diagram at strains of 0.55 and

0.85, the  $\xi$  value is the smallest when the strain rate is 1 and  $0.001~\rm s^{-1}$  at 953 K, respectively. Dynamic recovery and dynamic recrystallization occur when the alloy is deformed under specific deformation conditions.

### **5 Conclusions**

- (1) The deformation temperature and strain rate have significant influence on the microstructure evolution of the Cu-13Zn-1Ni-1Sn-1.5Al alloy during hot deformation. When the alloy is deformed at elevated temperature with high strain rate, the microstructure mainly consists of deformed grains, polygonized and recovery structures, and recrystallized grains. During high temperature deformation, the recrystallized grains are dominant.
- (2) The constitutive equation of the alloy at a true strain of 0.8 is  $\dot{\varepsilon}=7.22\times10^9\left[\sinh(0.0187\sigma)\right]^{3.67}$ . exp[-227.17/(*RT*)]. And the deformation activation energy is 227.17 kJ/mol.
- (3) Power dissipation and flow instability maps of the gold-imitation brass alloy at strains of 0.55 and 0.85 are established. According to the maps, the designed alloy shows good hot deformation property in the range of experimental temperature and strain rate. The recommended processing condition for hot compression is in the temperature range of  $1010-1040 \, \text{K}$  with a strain rate of  $1 \, \text{s}^{-1}$ .

### References

- [1] LI Zhou, XIAO Zhu, JIANG Yan-bin, LEI Qian, XIE Jian-xin. Composition design, phase transition and fabrication of copper alloys with high strength and electrical conductivity [J]. Transactions of Nonferrous Metals Society of China, 2019, 29: 2009–2049.
- [2] GENG Yong-feng, ZHANG Yi, SONG Ke-xing, JIA Yan-lin, LI Xu, STOCK H R, ZHOU Hong-lei, TIAN Bao-hong, LIU Yong, VOLINSKY A A, ZHANG Xiao-hui, LIU Ping, CHEN Xiao-hong. Effect of Ce addition on microstructure evolution and precipitation in Cu-Co-Si-Ti alloy during hot deformation [J]. Journal of Alloys and Compounds, 2020, 842: 155666.
- [3] SARKAR A, PRASAD M J N V, MURTY S V S N. Effect of initial grain size on hot deformation behaviour of Cu–Cr–Zr–Ti alloy [J]. Materials Characterization, 2020, 160: 110112.
- [4] SO S M, KIM K Y, LEE S J, YU Y J, LIM H A, OH M S. Effects of Sn content and hot deformation on microstructure and mechanical properties of binary high Sn content Cu-Sn

- alloys [J]. Materials Science and Engineering A, 2020, 796: 140054.
- [5] XIAO Zhu, LI Zhou, ZHU An-yin, ZHAO Yu-yuan, CHEN Jing-lin, ZHU Yun-tian. Surface characterization and corrosion behavior of a novel gold-imitation copper alloy with high tarnish resistance in salt spray environment [J]. Corrosion Science, 2013, 76: 42–51.
- [6] CHANG Ting-ru, HERTING G, JIN Ying, LEYGRAF C, ODNEVALL W I. The golden alloy Cu<sub>5</sub>Zn<sub>5</sub>Al<sub>1</sub>Sn: Patina evolution in chloride-containing atmospheres [J]. Corrosion Science, 2018, 133: 190–203.
- [7] CHEN J L, LI Z, ZHU A Y, LUO L Y, LIANG J. Corrosion behavior of novel imitation-gold copper alloy with rare earth in 3.5% NaCl solution [J]. Materials & Design, 2012, 34: 618–623.
- [8] YU Xiang-yu, XIAO Zhu, YU Qian, LI Zhou, LEI Qian, DAI Jie. Effect of Al on corrosion behavior of imitation-gold Cu–Zn–Ni–Sn alloys in 3.5 wt.% NaCl solution [J]. The JOM, 2021, 73: 589–599.
- [9] LIU Jia, WANG Xian-hui, LIU Ji-tuo, LIU Yan-feng, LI Hang-yu, WANG Chan. Hot deformation and dynamic recrystallization behavior of Cu-3Ti-3Ni-0.5Si alloy [J]. Journal of Alloys and Compounds, 2019, 782: 224-234.
- [10] WANG Meng-han, YANG Yong-chao, TU Shun-li, WEI Kang. A modified constitutive model and hot compression instability behavior of Cu–Ag alloy [J]. Transactions of Nonferrous Metals Society of China, 2019, 29: 764–774.
- [11] MA K, LIU Z Y, BI S, ZHANG X X, XIAO B L, MA Z Y. Microstructure evolution and hot deformation behavior of carbon nanotube reinforced 2009Al composite with bimodal grain structure [J]. Journal of Materials Science & Technology, 2021, 70: 73–82.
- [12] PARK C W, CHOI M S, LEE H, YOON J, JAVADINEJAD H R, KIM J H. High-temperature deformation behavior and microstructural evolution of as-cast and hot rolled β21S alloy during hot deformation [J]. Journal of Materials Research and Technology, 2020, 9: 13555–13569.
- [13] YANG Pei-ru, LIU Chen-xi, GUO Qian-ying, LIU Yong-chang. Variation of activation energy determined by a modified Arrhenius approach: Roles of dynamic recrystallization on the hot deformation of Ni-based superalloy [J]. Journal of Materials Science & Technology, 2021, 72: 162–171.
- [14] ZHU An-yin, CHEN Jing-lin, LI Zhou, LUO Li-yang, LEI Qian, ZHANG Liang, ZHANG Wan. Hot deformation behavior of novel imitation-gold copper alloy [J]. Transactions of Nonferrous Metals Society of China, 2013, 23: 1349–1355.
- [15] JIANG Ye-xin, WANG Xu, LI Zhou, XIAO Zhu, SHENG Xiao-fei, JIANG Hong-yun, CAI Geng-sheng, ZHANG Xian-wei. Microstructure evolution and hot deformation behavior of a CuNiSn alloy [J]. Processes, 2021, 9: 451.
- [16] WANG Xu, LI Zhou, XIAO Zhu, QIU Wen-ting. Microstructure evolution and hot deformation behavior of Cu-3Ti-0.1Zr alloy with ultra-high strength [J]. Transactions of Nonferrous Metals Society of China, 2020, 30: 2737-2748.
- [17] ZHANG Cun-sheng, WANG Cui-xue, GUO Ran, ZHAO Guo-qun, CHEN Liang, SUN Wen-chao, WANG Xie-bin.

- Investigation of dynamic recrystallization and modeling of microstructure evolution of an Al–Mg–Si aluminum alloy during high-temperature deformation [J]. Journal of Alloys and Compounds, 2019, 773: 59–70.
- [18] EBRAHIMI R, NAJAFIZADEH A. A new method for evaluation of friction in bulk metal forming [J]. Journal of Materials Processing Technology, 2004, 152: 136–143.
- [19] GOETZ R L, SEMIATIN S L. The adiabatic correction factor for deformation during the uniaxial compression test [J]. Journal of Materials Engineering and Performance, 2001, 10: 710-717.
- [20] LIANG Xiao-peng, LIU Yong, LI Hui-zhong, ZHOU Can-xu, XU Guo-fu. Constitutive relationship for high temperature deformation of powder metallurgy Ti-47Al-2Cr-2Nb-0.2W alloy [J]. Materials & Design, 2012, 37: 40-47.
- [21] MIRZADEH H, CABRERA J M, NAJAFIZADEH A. Constitutive relationships for hot deformation of austenite [J]. Acta Materialia, 2011, 59: 6441–6448.
- [22] ZHANG Yi, SUN Hui-li, VOLINSKY A A, WANG Bing-jie, TIAN Bao-hong, LIU Yong, SONG Ke-xing. Constitutive model for hot deformation of the Cu-Zr-Ce alloy [J]. Journal of Materials Engineering and Performance, 2018, 27: 728-738.
- [23] WANG Bing-jie, ZHANG Yi, TIAN Bao-hong, AN Jun-chao, VOLINSKY A A, SUN Hui-li, LIU Yong, SONG Ke-xing. Effects of Ce addition on the Cu-Mg-Fe alloy hot deformation behavior [J]. Vacuum, 2018, 155: 594-603.
- [24] GUO Jun-qing, YANG He, LIU Ping, CAI Zhi-wei. Hot deformation characterization and processing map of Cu-10%Fe-1.5%Ag in situ composite [J]. Rare Metals, 2017, 36: 912-918.
- [25] HUANG Dan, FENG Wei. Hot deformation characteristics and processing map of FV520B martensitic precipitation-

- hardened stainless steel [J]. Journal of Materials Engineering and Performance, 2019, 28: 2281–2291.
- [26] WANG Yong-xiao, ZHAO Guo-qun, XU Xiao, CHEN Xiao-xue, ZHANG Cun-sheng. Constitutive modeling, processing map establishment and microstructure analysis of spray deposited Al-Cu-Li alloy 2195 [J]. Journal of Alloys and Compounds, 2019, 779: 735–751.
- [27] XI Tong, YIN Lu, YANG Chun-guang, YANG Ke. Hot deformation behavior and processing map of a Cu-dearing 2205 duplex stainless steel [J]. Acta Metallurgica Sinica (English Letters), 2019, 32: 1537–1548.
- [28] PRASAD Y V R K, GEGEL H L, DORAIVELU S M, MALAS J C, MORGAN J T, LARK K A, BARKER D R. Modeling of dynamic material behavior in hot deformation: Forging of Ti-6242 [J]. Metallurgical Transactions A, 1984, 15: 1883–1892.
- [29] PRASAD Y V R K, RAO K P. Processing maps and rate controlling mechanisms of hot deformation of electrolytic tough pitch copper in the temperature range 300–950 °C [J]. Materials Science and Engineering A, 2005, 391: 141–150.
- [30] MURTY S V S N, RAO B N. On the development of instability criteria during hotworking with reference to IN718 [J]. Materials Science and Engineering A, 1998, 254: 76–82.
- [31] LI Chang-min, HUANG Liang, ZHAO Ming-jie, ZHANG Xiao-ting, LI Jian-jun, LI Peng-chuan. Influence of hot deformation on dynamic recrystallization behavior of 300M steel: Rules and modeling [J]. Materials Science and Engineering A, 2020, 797: 139925.
- [32] LIN Y C, CHEN X M. A critical review of experimental results and constitutive descriptions for metals and alloys in hot working [J]. Materials & Design, 2011, 32: 1733–1759.

# 高耐蚀仿金黄铜合金的热变形行为及显微组织演变

于翔宇, 肖 柱, 李 周, 赵辛巳, 陆思见, 傅原圆

中南大学 材料科学与工程学院,长沙 410083

摘 要:通过热压缩实验研究 Cu-13Zn-1Ni-1Sn-1.5Al 仿金黄铜在温度为 953~1123 K 和应变速率为  $0.001\sim1$  s<sup>-1</sup> 条件下的热变形特征。应力-应变曲线表明,流动应力随着温度的升高和应变速率的降低而降低。在 0.01 s<sup>-1</sup> 的恒定应变速率下,当温度达到 1073 K 时,合金的显微组织中出现动态再结晶晶粒。建立合金在不同应变( $\varepsilon$ =0.1, 0.2, 0.3, 0.4, 0.5, 0.6, 0.7, 0.8)条件下的本构方程并计算其变形激活能。当应变为 0.8 时,合金的本构方程为= $7.22\times10^9$ [sinh( $0.0187\sigma$ )]<sup>3.67</sup>exp[-227.17/(RT)],变形激活能为 227.17 kJ/mol。绘制仿金合金在不同应变条件下的功率耗散图和失稳图,得到合金在热压缩工艺中的最佳热变形温度范围为  $1010\sim1040$  K,应变速率为 1 s<sup>-1</sup>。 **关键词**:仿金黄铜合金,热变形行为;动态回复;动态再结晶

(Edited by Wei-ping CHEN)